Effects of boundary conditions on bistable behaviour in axisymmetrical shallow shells

P. M. Sobota and K. A. Seffen

Department of Engineering, University of Cambridge, Trumpington Street, Cambridge CB2 1PZ, United Kingdom

Author for correspondence:
K. A. Seffen
e-mail: kas14@cam.ac.uk

Subject areas:
structural engineering, solid mechanics

Keywords:
bistability, Föppl-von Kármán, large deflection shells, morphing structures, post-buckling analysis, analytical approach

Abstract
Multistable shells are thin-walled structures that have more than one stable state of self-stress. We consider isotropic axisymmetrical shallow shells of arbitrary polynomial shapes using a Föppl-von Kármán analytical model. By employing a Rayleigh-Ritz approach, we identify stable shapes from local minima in the strain energy formulation, and we formally characterise the level of influence of the boundary conditions on the critical geometry for achieving bistable inversion—an effect not directly answered in the literature. Systematic insight is afforded by connecting the boundary to ground through sets of extensional and rotational linear springs. For typical cap-like shells, it is shown that bistability is generally enhanced when the extensional spring stiffness increases and when the rotational spring stiffness decreases *i.e.* when boundary movements in-plane are resisted but when their rotations are not; however, for certain other shapes and large in-plane stiffness values, bistability can be enhanced by resisting but not entirely preventing edge rotations. Our predictions are furnished as detailed regime maps of the critical geometry, which are accurately correlated against finite element analysis. Furthermore, the suitability of single degree-of-freedom models, for which solutions are achieved in closed form, are evaluated and compared to our more accurate predictions.

1. Introduction

Multistability in shells arises from the interaction of out-of-plane bending and in-plane stretching. A bistable example from Nature is the Venus Flytrap, which can rapidly "snap-through" and close from an open equilibrium position to ensnare prey [1]; artificial applications range from familiar objects such as flick bracelets and thermostatic switches in kettles [2] to semi-conductors in the field of microelectronics [3], and to recent innovations in energy harvesting devices [4] or deployable spacecraft elements [5].

Fundamental research on bistable structures was first undertaken by Timoshenko [6] for curved beams, and by Wittrick *et al.* [2] as well as Hyer [7] for shells. Since multistability in general is concomitant with large deflections, the non-linear and coupled Föppl-von Kármán (FvK) theory of shallow shell elastic deformation [8] provides a suitable theoretical framework for ascertaining their behaviour. For more intricate shells with bespoke support conditions, the finite element (FE) method enables their analysis straightforwardly but not without computational expense or the complete assurance that all possible stable states have been detected. Correspondingly,

the FvK framework remains competitive and affords direct insight into the factors which govern multistability. Often, its governing equations can be intractable unless simplifying assumptions about the shape of shell are made. One successful approach describes the dominant deflections by *uniform* curvatures and twisting curvatures for the sake of simplicity. Approximating the shape globally this way, however, fails to capture local edge effects [9], leading typically to a non-vanishing bending moment at the boundary. Despite this, the uniform curvature (UC) approach provides a good approximation ($\approx \pm 10\%$) of the ratio of bending-to-stretching energies for shells with constant thickness (*e.g.* [2;3;7;10–13]), which is suitable for most design purposes. For a lenticular shell, where a vanishing thickness precludes edge effects, Mansfield [14] obtains an exact solution for "extra" *i.e.* bistable states.

More detailed numerical approaches use higher-order polynomial basis functions for describing the large deflection shape of shells with greater accuracy [15;16]. Other elaborate analytical models also consider higher-order curvatures, for example, Vidoli [17] demonstrates the increased accuracy of models with three degrees-of-freedom and a quadratically varying curvature (QVC). Other recent approaches show that the snap-through processes of magnetically actuated caps [18] or the multistable behaviour of a one-sided clamped plate [19] can be captured analytically with higher-order models. To some extent, these models show superior accuracy because a violation of the out-of-plane boundary condition (BC) is minimised at least or completely prevented.

In this paper, we consider the bistable behaviour of linear elastic, axisymmetrical shallow shells using polynomial displacement fields. One aim is to establish the trade-off between performance accuracy and model complexity as the polynomial order is increased. By enforcing axisymmetry and thus displacement fields that only vary radially, our analysis is simplified without compromising the generality of results. Our main aim, however, is to explore the effect that support conditions have upon the bistable character since the capability of any multistable structure is realised only by connecting it externally. Not only do we couple to the first aim insofar as capturing these boundary conditions exactly (where the UC model is obliged to neglect the edge moment), we may observe if bistability is directly enhanced or eroded by the nature of the external connection—in this case—to ground. This has not been formally addressed although some researchers have dealt with the "limits" of connectivity, where an edge is pinned or clamped as part of their particular study, and others have noted the importance of particular support conditions in stability problems experimentally [20]. We offer a broader sense of performance by implementing linear elastic connections of arbitrary stiffness, which behave as spring-like foundational elements.

Our approach derives a strain energy potential for the deformed shell whose stable equilibria are identified by familiar calculus of variations. We seek load-free, statical configurations without considering the unstable transition between them, and we use three examples to highlight the effectiveness of our methodology. The first is a familiar spherical cap, which is mounted on "pinned" rollers at its edge so that bistable inversion takes place without constraint. This example can be directly compared to similar caps in the literature, and we determine the critical geometry at which bistable inversion *just* becomes possible in terms of the minimum height of the cap relative to its thickness.

In the second example, linear springs connect the roller supports of the first cap to ground. These springs apply radial forces to the cap that resist in-plane displacements at the edge, where in-plane radial stresses are no longer zero. Despite this simple modification in how the cap is supported, the critical height is found to decrease in a non-linear fashion as the stiffness increases. In the final example, rotations of the shell boundary are resisted by torsional springs that locally apply a radial bending moment. We consider a non-uniformly curved shell initially with no boundary gradient but having some height because this allows us to solve efficaciously for the deformed shape by superposing two deflection fields with specific edge characteristics: one with zero bending moment, the other with zero slope. The contributions from each field are obtained by matching the actual bending moment and rotation of the cap edge to the spring element. This approach is novel and affords a reasonably compact working compared to

one that uses a general polynomial displacement field *e.g.* as in Wittrick *et al.*[2]. This shell is also supported on in-plane extensional springs for a completely sprung boundary and, hence, broader insight. A non-linear performance of the critical geometry is revealed where we can observe, for example, the effect of the limits of connectivity for stiffness extrema. We constrained our investigations to closed shells consisting of isotropic materials with external connections at the *edge*, but point out possible extensions for more complex constitutive laws[21;22], support conditions[23;24], or geometries[25] (e.g. polar-orthotropic annuli on elastic foundations).

The structure of this paper is as follows. In the next section, we derive the general and particular solutions of the FvK governing equations. All results are then compared to finite element simulations in §3, where we emphasise the stark relevances of different boundary conditions; the FE model is briefly described in this section. A summary and outlook follows in §4.

2. Analytical formulation

We undertake a higher-order Rayleigh-Ritz method that extends previous UC models for load-free shells *e.g.* as found in Seffen & McMahon[26]. A systematic overview of the approach is given in Fig. 1, which is elaborated next.

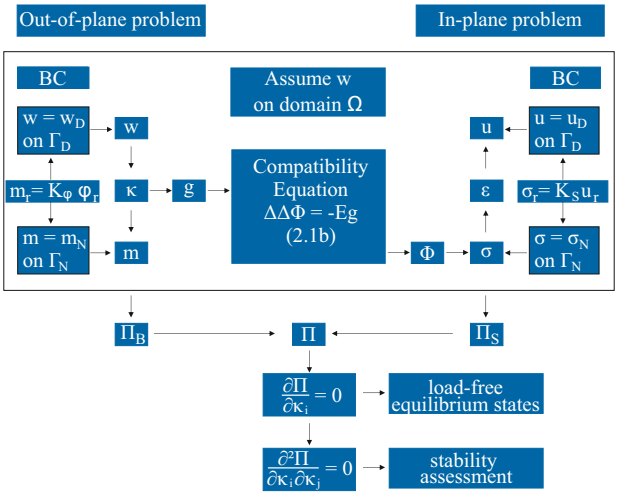

Figure 1. Overview of the coupled nature of the Föppl-von Kármán equations and our Rayleigh-Ritz solution approach.

By assuming a polynomial expression of the transverse deflection field, w, on a domain Ω over the shell with boundary, Γ, we describe the curvatures, κ, the deflection gradients, φ_r, the bending moment, m, the Gaussian curvature, g, as well as the bending energy, Π_B, in terms of n degrees-of-freedom (DOF). Out-of-plane curving is coupled to the in-plane stresses by relating the change in Gaussian curvature to the Airy stress function, Φ, using Gauss's Theorema Egregium[9]. From Φ, the in-plane stress resultants, σ, the mid-plane strains, ε, as well as the displacement, u, and stretching energy, Π_S, are derived, whilst satisfying the in-plane boundary conditions. Finally, stable configurations are identified by minimising the total strain energy, Π equal to $\Pi_B + \Pi_S$. The general solution is given next; the particular solution, which elucidates satisfaction of the boundary conditions on Γ, is given afterwards.

(a) General solution

Our shell is axisymmetrical and can be connected to ground everywhere along its circumference by linear elastic springs. Because deformations are also assumed to be axisymmetrical, the springs resist in-plane extensions and out-of-plane rotations of the shell boundary purely in the radial direction without circumferential variation. A shallow spherical segment is depicted in Fig. 2(a), with a through-thickness, t, and an outer planform radius, a. We choose this segment only to illustrate more easily the cylindrical coordinate field given by r and θ, and by z in the direction of transverse w. For a radial variation alone and no initial deflections, the Föppl-von Kármán plate equations can be written as[27;28]:

$$D\nabla^4 w - \frac{t}{r}\frac{\mathrm{d}}{\mathrm{d}r}\left[\frac{\mathrm{d}w}{\mathrm{d}r}\frac{\mathrm{d}\Phi}{\mathrm{d}r}\right] = q \qquad (2.1a) \qquad\qquad \frac{1}{E}\nabla^4\Phi + \frac{1}{r}\frac{\mathrm{d}w}{\mathrm{d}r}\frac{\mathrm{d}^2 w}{\mathrm{d}r^2} = 0\,, \qquad (2.1b)$$

where ∇^2 is the familiar Laplacian operator, equal to $\mathrm{d}^2(..)/\mathrm{d}r^2 + (1/r)\mathrm{d}(..)/\mathrm{d}r$.

These expressions are non-linear and coupled, and are valid only when the radial curvatures, $\kappa_r \ll 1/t$, and the gradient of the shell, $\mathrm{d}w/\mathrm{d}r \ll 1$, everywhere. The external transverse pressure load is denoted by q, and the flexural rigidity is $D = Et^3/[12(1-\nu^2)]$, with Young's modulus, E, and Poisson's ratio, ν. Even though large out-of-plane deflections are considered, the shallow shell condition arises because the strain formulation

$$\varepsilon_r = \frac{\mathrm{d}u_r}{\mathrm{d}r} + \frac{1}{2}\left(\frac{\mathrm{d}w}{\mathrm{d}r}\right)^2 \qquad \text{and} \qquad \varepsilon_\theta = \frac{u_r}{r}\,, \qquad (2.2)$$

is not invariant under rotation since it neglects large in-plane displacements. In order to decouple Eqns (2.1a) and (2.1b), we first solve the "out-of-plane" problem depending on w, and later define a surjective and not injective stress function, $\Phi(w)$, which implies that there is not a unique inverse function, $w(\Phi)$.

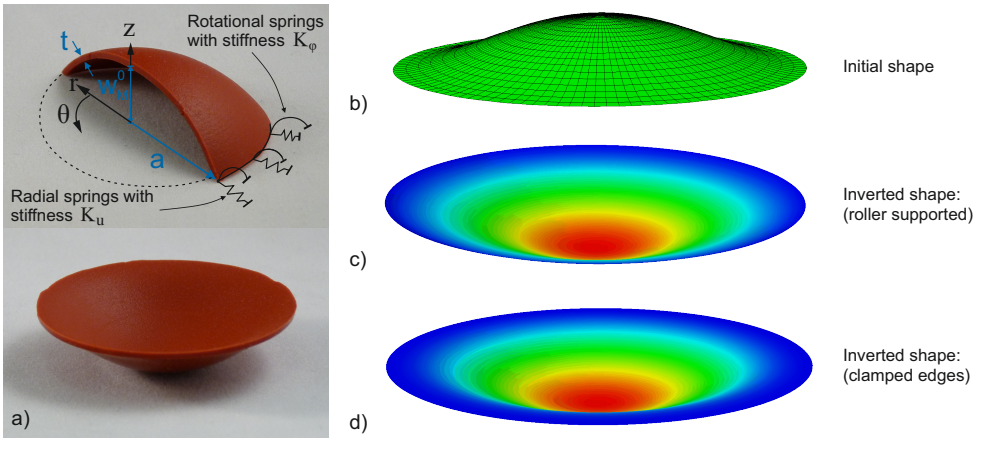

Figure 2. a) Cutaway view of a cap mounted on spring supports in a cylindrical coordinate system (r, θ, z) with an initial midpoint deflection w_M^0 (top), and corresponding inverted shape for roller supported edges (bottom); this particular shape is monostable if the edges are instead clamped. b) Geometrically non-linear finite element simulations using ABAQUS[29] of a shell with an initial non-uniform deflection according to Eqn (2.14b). Inverted configurations for roller supported (free) edges and for clamped edges are shown in c) and d), respectively, where colour contours indicate transverse deflection levels.

Remark 1. The equilibrium equation, (2.1a), is in general not satisfied for polynomial approaches of w and Φ with a finite number of terms. For an alternative state of self-stress, q is absent, and hence, for a deflection field, w, of order $p > 1$, the first term in Eqn (2.1a) is of order $p-4$, whilst the second terms order is $p - 3 + \deg(\mathrm{d}\Phi/\mathrm{d}r)$. For matching orders, the Airy

stress function, Φ, has a logarithmic component to enforce the compatibility for the highest order term in Eqn (2.1a); however, such an Airy stress function invokes the incompatible behaviour of infinite strain energy due to infinite stress peaks at the centre of the plate [*c.f.* Eqn (2.6)]. This problem cannot be overcome by increasing the number of terms, since every additional term also requires an additional correction term, and a mismatch always remains. In contrast, polynomial approaches are suitable for the second FvK equation, (2.1b), with $2 \cdot \deg(w) = \deg(\Phi)$. Since equilibrium has the same axiomatic nature as work, we ignore the equilibrium equation, (2.1a), by assuming some (as yet unknown) deflection instead, and find an approximate *yet* accurate solution via energy minimisation.

(i) Out-of-plane curving

The initially stress-free shape, w^0, is distinguished from the current shape, w, by a superscript 0; it is specified by a function $f^0(r)\, w_M^0$, where w_M^0 is the initial midpoint deflection. The *change* between the two configurations is denoted by a hat, so the deflection reads $\hat{w} = w - w^0$. We focus on finding alternative equilibrium configurations that are load-free even though a load is needed to marshal the actual transition. We therefore substitute the load with a "forcing term" of the deflection

$$\hat{w} = \hat{f}(r)\, \hat{w}_M\,; \tag{2.3}$$

$\hat{f}(r)$, as well as $f^0(r)$, is an arbitrary polynomial expression of order p, and both are specified in §2(b). For axisymmetrical structures, the change in gradient, $\hat{\varphi}_r$, radial curvature, $\hat{\kappa}_r$, as well as hoop-wise curvature, $\hat{\kappa}_\theta$, are derived from the definition of the deflection via

$$\hat{\varphi}_r = -\frac{\mathrm{d}\hat{w}}{\mathrm{d}\,r} \quad , \quad \hat{\kappa}_r = -\frac{\mathrm{d}^2\hat{w}}{\mathrm{d}\,r^2} \quad \text{and} \quad \hat{\kappa}_\theta = -\frac{1}{r}\frac{\mathrm{d}\hat{w}}{\mathrm{d}\,r}. \tag{2.4}$$

Since the initial configuration is stress free, the principal bending moments, m_r and m_θ, as well as the shear force, q_r, are independent of the initial configuration, so the change in these values corresponds to the current value, *i.e.* $\hat{m}_r = m_r$. For linear elastic, isotropic constitutive behaviour, these read:

$$m_r = D\,(\hat{\kappa}_r + \nu\hat{\kappa}_\theta) \quad , \quad m_\theta = D\,(\hat{\kappa}_\theta + \nu\hat{\kappa}_r) \quad \text{and} \quad q_r = \frac{\mathrm{d}m_r}{\mathrm{d}r} + \frac{m_r - m_\theta}{r}\,. \tag{2.5}$$

(ii) In-plane stretching

The Airy stress function, Φ, is a bi-potential function for describing the mid-plane stress resultants as

$$\sigma_r = \frac{1}{r}\frac{\mathrm{d}\Phi}{\mathrm{d}r} \qquad \text{and} \qquad \sigma_\theta = \frac{\mathrm{d}^2\Phi}{\mathrm{d}r^2}\,. \tag{2.6}$$

The corresponding strains are connected via the constitutive law

$$\varepsilon_r = \frac{1}{E}\,(\sigma_r - \nu\sigma_\theta) \qquad \text{and} \qquad \varepsilon_\theta = \frac{1}{E}\,(\sigma_\theta - \nu\sigma_r)\,, \tag{2.7}$$

and using the same relation with initial values leads to $\varepsilon_r^0 = \varepsilon_\theta^0 = 0$. By transforming either the radial or circumferential strains from Eqn (2.2), the radial displacement is expressed either in terms of the in-plane strains and the out-of-plane deflections, or solely in terms of in-plane variables, respectively:

$$u_r = \int \varepsilon_r\,\mathrm{d}r - \frac{1}{2}\int \left(\frac{\mathrm{d}w}{\mathrm{d}r}\right)^2 - \left(\frac{\mathrm{d}w^0}{\mathrm{d}r}\right)^2 \mathrm{d}r\,, \qquad \text{or} \qquad u_r = r\,\varepsilon_\theta\,. \tag{2.8}$$

(iii) Bending-stretching interaction

The in-plane and out-of-plane responses are connected by equating the extrinsic definition of Gaussian curvature to in-plane strains according to Gauss's Theorema Egregium[9]:

$$g = \kappa_r \kappa_\theta = \frac{1}{r}\frac{\mathrm{d}\varepsilon_r}{\mathrm{d}r} - \frac{1}{r}\frac{\mathrm{d}^2(r\,\varepsilon_\theta)}{\mathrm{d}r^2}\,. \tag{2.9}$$

Since the initial configuration is stress free, the change in the Airy stress function equals the current value ($\Phi = \hat{\Phi}$), and by substituting Eqn (2.6) into Eqn (2.7), Eqn (2.9) can be rewritten as

$$-E\hat{g} = \frac{\mathrm{d}^4\Phi}{\mathrm{d}r^4} + \frac{2}{r}\frac{\mathrm{d}^3\Phi}{\mathrm{d}r^3} - \frac{1}{r^2}\frac{\mathrm{d}^2\Phi}{\mathrm{d}r^2} + \frac{1}{r^3}\frac{\mathrm{d}\Phi}{\mathrm{d}r}\,, \tag{2.10}$$

where $\hat{g}$ is the *change* in Gaussian curvature

$$\hat{g} = g - g^0 = \kappa_r\kappa_\theta - \kappa_r^0\kappa_\theta^0\,, \tag{2.11}$$

which is a polynomial expression of order $2p-4$ in r. By introducing the coefficients α_i, this term can be sorted by order:

$$\hat{g} = \sum_{i=0}^{2p-4} \alpha_i \left(\frac{r}{a}\right)^i\,, \tag{2.12}$$

which facilitates a succinct notation of the corresponding Airy stress function after substituting Eqn (2.12) into Eqn (2.10) and integrating with respect to r:

$$\Phi = E\sum_{i=0}^{2p-4} \frac{\alpha_i\, r^4}{(i+2)^2(i+4)^2}\left(\frac{r}{a}\right)^i + \frac{1}{2}C_1 r^2 + C_2\log(r) + \frac{1}{2}C_3 r^2\left[\log(r) - \frac{1}{2}\right]\,. \tag{2.13}$$

The relevant constants of integration C_1, C_2 and C_3 are now used to satisfy the in-plane boundary conditions.

(b) Particular solution

Whilst the initial shape can have the form of any arbitrary polynomial expression, we choose approximations of two very well known examples for evaluation in §3 and enforce zero displacement at $r = a$:

$$w^0 = \left(1-\rho^2\right) w_M^0 \qquad (2.14a) \qquad \text{or} \qquad w^0 = \left(1-\rho^2\right)^2 w_M^0\,, \qquad (2.14b)$$

where w_M^0 denotes the initial midpoint deflection, and ρ the dimensionless radius r/a. Shape a) resembles a uniformly curved shallow cap and is inspired by a study of initially curved bistable beams[6] using a half cosine-wave; b) represents a full cosine wave akin to the deflection field of a plate with a clamped edge[30–32], where the gradient is zero. These shells are subjected to two possible types of boundary conditions: Dirichlet boundary conditions, which impose displacements or rotations on a boundary Γ_D, and Neumann boundary conditions, which prescribe generalised stresses on Γ_N. When springs are connected to the boundary, these conditions become coupled, and the specific stresses (from in-plane forces or bending moments) are related to an in-plane displacement or rotation via the spring stiffness, K_u or K_φ, respectively, by

$$-t\sigma_r = K_u\, u_r \qquad (2.15a) \qquad \text{and} \qquad -m_r = K_\varphi\,\hat{\varphi}_r\,. \qquad (2.15b)$$

The minus sign in both expressions accords a resistive force or bending moment for positive directions of u_r and $\hat{\varphi}_r$. Allowing for the use of springs, the complete range of physical supports

can be established by combining two out-of-plane boundary conditions and one additional in-plane condition as follows:

$$\text{roller support:} \quad w=0, \quad m_r=0, \quad \sigma_r=0 \tag{2.16a}$$

$$\text{pinned spring support:} \quad w=0, \quad m_r=0, \quad -t\sigma_r=K_u\,u_r \tag{2.16b}$$

$$\text{dual spring support:} \quad w=0, \quad -m_r=K_\varphi\,\hat{\varphi}_r\,, \quad -t\sigma_r=K_u\,u_r \tag{2.16c}$$

$$\text{fixed pinned support:} \quad w=0, \quad m_r=0, \quad u_r=0 \tag{2.16d}$$

$$\text{clamped support:} \quad w=0, \quad \hat{\varphi}_r=0, \quad u_r=0 \tag{2.16e}$$

$$\text{continuous plate at } r=0\text{:} \quad q_r=0, \quad \hat{\varphi}_r=0, \quad u_r=0 \tag{2.16f}$$

The first three supports are directly employed in the examples of §3. The fixed pinned support and the clamped support are equivalent to having infinite spring stiffness, so by letting K_u and K_φ tend to large values in Eqns (2.16*b*) and (2.16*c*), we may observe how the ideal support conditions are approached from a "spring" perspective. The final condition ensures that we deal with plates without central holes: if we wished to consider planform annuli, we may substitute this final condition with one from any of the five expressions above it but written in terms of the inner radius of the hole, see Sobota & Seffen [25] for details.

(i) Out-of-plane bending

In order to describe the transverse deflections of a shell bounded by rotational springs, $\hat{w}$ is subdivided into two fields where the edge is either free to rotate giving a "hinged" *i.e.* pinned deflection field, $\hat{w}^h$, or is fixed to yield deflections, $\hat{w}^c$. The first field is a polynomial series with n degrees-of-freedom, η_i, which by itself is the solution for cases where the boundary of shell is pinned for all time. The rotational spring equation, Eqn (2.15*b*), prescribes the compatibility between these two fields and is later used to express the clamped midpoint deflection, $\hat{w}^c_M$, in terms of the n degrees-of-freedom, η_i, *c.f.* Eqn (2.26). Correspondingly, the total midpoint deflection is $\hat{w}_M=(\hat{w}^h+\hat{w}^c)|_{\rho=0}$, which is now computed according to the scheme in Fig. 3.

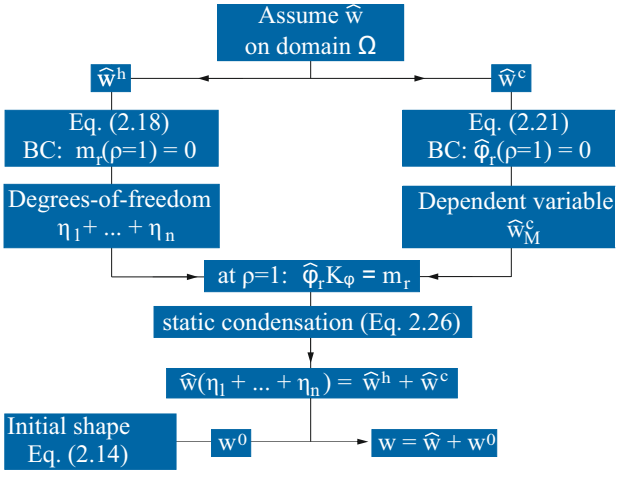

Figure 3. Schematic of the formulation of the deflection field components.

Hinged subset

The hinged subset has to satisfy the boundary conditions of a vanishing bending moment and deflection at $\rho=1$. To ensure this, we combine Eqn (2.4) with Eqn (2.5) and choose a polynomial

series of even powers for the radial bending moment, *i.e.*

$$D\left[-\frac{\mathrm{d}^2\hat{w}^h}{\mathrm{d}\,r^2}-\nu\frac{1}{r}\frac{\mathrm{d}\hat{w}^h}{\mathrm{d}\,r}\right]=\frac{D}{a^2}\sum_{i=1}^{n}\left[1-\rho^{2i}\right]\eta_i\,. \tag{2.17}$$

Solving this differential equation gives the hinged deflection field, of order $p=2n+2$, as

$$\hat{w}^h=\sum_{i=1}^{n}\frac{1}{2}\left[\frac{1-\rho^2}{1+\nu}-\frac{1-\rho^{2i+2}}{(i+1)(1+2i+\nu)}\right]\eta_i\,, \tag{2.18}$$

where the constant of integration enforces $\hat{w}^h|_{\rho=1}=0$. From this we can determine the change in curvatures and the radial gradient

$$\hat{\kappa}_r^h=\sum_{i=1}^{n}\left[\frac{1}{1+\nu}-\frac{1+2i}{1+2i+\nu}\rho^{2i}\right]\frac{\eta_i}{a^2}\quad,\quad\hat{\kappa}_\theta^h=\sum_{i=1}^{n}\left[\frac{1}{1+\nu}-\frac{1}{1+2i+\nu}\rho^{2i}\right]\frac{\eta_i}{a^2}\quad\text{and}\quad\hat{\varphi}_r^h=r\,\hat{\kappa}_\theta^h, \tag{2.19}$$

as well as the radial- and circumferential bending moments

$$m_r^h=D\sum_{i=1}^{n}\left[1-\rho^{2i}\right]\frac{\eta_i}{a^2}\quad\text{and}\quad m_\theta^h=D\sum_{i=1}^{n}\left[1-\frac{1+\nu+2\nu i}{1+2i+\nu}\rho^{2i}\right]\frac{\eta_i}{a^2}\,. \tag{2.20}$$

For a single degree-of-freedom, η_1, these curvature and bending moment expressions have a quadratic variation in ρ.

Clamped subset

The clamped subset is chosen to be[30;32]:

$$\hat{w}^c=\left(1-\rho^2\right)^2\,\hat{w}_M^c\,. \tag{2.21}$$

According to Eqn (2.4), the corresponding change in gradient and curvatures read:

$$\hat{\varphi}_r^c=4\rho\left(1-\rho^2\right)^2\frac{\hat{w}_M^c}{a}\quad,\quad\hat{\kappa}_r^c=4\left(3\rho^2-1\right)\frac{\hat{w}_M^c}{a^2}\quad\text{and}\quad\hat{\kappa}_\theta^c=4\left(\rho^2-1\right)\frac{\hat{w}_M^c}{a^2}\,. \tag{2.22}$$

From Eqn (2.5), we deduce

$$m_r^c=4D\left(\rho^2(3+\nu)-\nu-1\right)\frac{\hat{w}_M^c}{a^2}\quad\text{and}\quad m_\theta^c=4D\left(\rho^2(1+3\nu)-\nu-1\right)\frac{\hat{w}_M^c}{a^2}\,, \tag{2.23}$$

and confirm that the radial bending moment on the edge is generally non-zero for $\rho=1$. Note also that the two conditions concerning the deflection in Eqn (2.16*e*) are satisfied for arbitrary values of the midpoint deflection $\hat{w}_M^c$ in the clamped deflection field, $\hat{w}^c$. Summing this expression with the initial deflection, w^0, and the hinged deflection, $\hat{w}^h$, leads to the current configuration, $w=w^0+\hat{w}^h+\hat{w}^c$.

Resulting deflection field $\hat{w}$

From the boundary conditions of the hinged and clamped fields, only the former contributes to a change of gradient at $\rho=1$, which enables us to find $\hat{\varphi}_r$:

$$\hat{\varphi}_r\Big|_{\rho=1}=\sum_{i=1}^{n}\left[\frac{1}{1+\nu}-\frac{2i}{1+2i+\nu}\right]\frac{\eta_i}{a}\,. \tag{2.24}$$

At $\rho=1$, $m_r=0$ for the hinged subset, so the bending moment is solely evoked by the clamped part in Eqn (2.23):

$$m_r\Big|_{\rho=1}=-8D\,\frac{\hat{w}_M^c}{a^2}\,. \tag{2.25}$$

Substituting both of these expressions into the rotational spring equation, Eqn (2.15*b*), we can solve for

$$\hat{w}_M^c = -\frac{K_\varphi}{8D}\,\hat{\varphi}_r\bigg|_{\rho=1} = \frac{K_\varphi\, a}{8D}\sum_{i=1}^{n}\left[\frac{-1}{1+\nu}+\frac{2i}{1+2i+\nu}\right]\eta_i\,, \tag{2.26}$$

which enforces the compatibility of the hinged and clamped deformation modes. The edge bending moment for the clamped mode is now related to the rotation of the hinged deflection field, and $\hat{w}_M^c$ is now expressed in terms of the n hinged degrees-of-freedom, η_i. For a vanishing spring stiffness, $K_\varphi = 0$, the clamped part vanishes; for K_φ tending to infinity, the edge rotation becomes very small but is not allowed to vanish because the solution is achieved with respect to the hinged degrees-of-freedom. The consequences of this assumption are addressed in §3.

Remark 2. For roller supported caps, a uniform curvature approach is also investigated in this paper by setting $\hat{w} = \rho^2 \hat{w}_M$, where the midpoint deflection, $\hat{w}_M = \eta_1$, serves as a single degree-of-freedom.

Remark 3. The midpoint deflection of the clamped mode is expressed in terms of η_i from Eqn (2.26) for n degrees-of-freedom but where the corresponding deflection variation in ρ is always of order four, *c.f.* Eqn (2.21). For the hinged mode in Eqn (2.18), the variation in ρ increases with n, up to order $2n+2$. We do not impose a similar polynomial expansion in ρ for the clamped mode because we find that it is simply not needed in view of producing accurate results.

(ii) Bending-stretching interaction

The change in Gaussian curvature is calculated according to Eqn (2.11) with $\kappa_r = \kappa_r^0 + \hat{\kappa}_r^h + \hat{\kappa}_r^c$ and $\kappa_\theta = \kappa_\theta^0 + \hat{\kappa}_\theta^h + \hat{\kappa}_\theta^c$. Because these expressions become rather convoluted with increasing order, we refer the reader to the Appendix where the values for κ_r, κ_θ, $\hat{g}$ and the corresponding α_i terms, Eqn (2.12), are given for a three degree-of-freedom model with rotational edge springs; lower-order models are straightforward to derive from these expressions by setting "unused" degrees-of-freedom to zero. Since the product of initial curvatures also features in $\hat{g}$, the α_i terms are given for both initial shapes expressed by Eqn (2.14*a*) and (2.14*b*). For instance, the curvatures for a hinged ($K_\varphi = 0$), uniformly curved cap initially ($\kappa_r^0 = \kappa_\theta^0 = 2w_M^0/a^2$) with a single degree-of-freedom ($n=1$) are equal to

$$\kappa_r = \frac{1}{a^2}\left[\frac{w_M^0}{2}+\eta_1\left(\frac{1}{\nu+1}-\frac{3\rho^2}{\nu+3}\right)\right] \quad \text{and} \quad \kappa_\theta = \frac{1}{a^2}\left[\frac{w_M^0}{2}+\eta_1\left(\frac{1}{\nu+1}-\frac{\rho^2}{\nu+3}\right)\right], \tag{2.27}$$

which are both quadratic variations in ρ, leading to a change in Gaussian curvature:

$$\hat{g} = \frac{1}{a^4}\left[\frac{w_M^0}{2}+\eta_1\left(\frac{1}{\nu+1}-\frac{3\rho^2}{\nu+3}\right)\right]\left[\frac{w_M^0}{2}+\eta_1\left(\frac{1}{\nu+1}-\frac{\rho^2}{\nu+3}\right)\right]-\left(\frac{w_M^0}{2\,a^2}\right)^2. \tag{2.28}$$

The α_i terms, Eqn (2.12), with $2p-4 = 4n\ (=4)$now read:

$$\alpha_0 = \frac{\left(2\eta_1+(1+\nu)w_M^0\right)^2}{4a^4(1+\nu)^2}\,, \quad \alpha_2 = -\frac{2\eta_1\left(2\eta_1+(1+\nu)w_M^0\right)}{a^4(\nu+1)(\nu+3)}\,, \quad \alpha_4 = \frac{3\eta_1^2}{a^4(\nu+3)^2}\,. \tag{2.29}$$

Note that in this particular case $\hat{w}_M^c = 0$ follows from Eqn (2.26) with $K_\varphi = 0$, which ought to be expected.

(iii) In-plane stretching

From the Airy stress function in Eqn (2.13), the in-plane stresses are calculated via Eqn (2.6) to be:

$$\begin{aligned}\sigma_r &= E\sum_{i=0}^{2p-4}\frac{\alpha_i\rho^{i+2}a^2}{(i+2)^2(i+4)} + C_1 + \frac{C_2}{a^2\rho^2} + C_3[\log(\rho)+\log(a)],\\ \sigma_\theta &= E\sum_{i=0}^{2p-4}\frac{\alpha_i(i+3)\rho^{i+2}a^2}{(i+2)^2(i+4)} + C_1 - \frac{C_2}{a^2\rho^2} + C_3[1+\log(\rho)+\log(a)]\,.\end{aligned} \tag{2.30}$$

At $\rho=0$, the constants C_2 and C_3 have to be zero and, thus, Eqn (2.30) is simplified to

$$\sigma_r = \sigma_{\alpha r} + C_1 \qquad \text{and} \qquad \sigma_\theta = \sigma_{\alpha\theta} + C_1\,, \tag{2.31}$$

where $\sigma_{\alpha r}$ and $\sigma_{\alpha\theta}$ denote the summation terms with α_i. These expressions also satisfy the condition $u_r|_{\rho=0}=0$, which is equivalent to having a biaxial stress state, $\sigma_r=\sigma_\theta$, at the centre of the plate. The remaining constant C_1 is determined for a linear elastic in-plane extensional spring by using $u_r = r\varepsilon_\theta$ with

$$\varepsilon_\theta = \frac{1}{E}\left(\sigma_{\alpha\theta} - \nu\sigma_{\alpha r} + (1-\nu)\,C_1\right), \tag{2.32}$$

and substituting σ_r from Eqn (2.31) into the extensional spring relationship, Eqn (2.15a), with $\rho=1$ gives:

$$C_1 = -\frac{E\,t\,\sigma_{\alpha r} + K_u\,a\,(\sigma_{\alpha\theta} - \nu\,\sigma_{\alpha r})}{E\,t + K_u\,a\,(1-\nu)}\bigg|_{\rho=1}\,. \tag{2.33}$$

For the limit of a vanishing or infinite stiffness, this expression simplifies to

$$C_1 = -\sigma_{\alpha r}\,\big|_{\rho=1} \quad \text{for } K_u=0 \quad \text{or} \quad C_1 = -\frac{E}{a}u_{\alpha r}\,\big|_{\rho=1} = -\frac{\sigma_{\alpha\theta}-\nu\,\sigma_{\alpha r}}{1-\nu}\bigg|_{\rho=1} \quad \text{for } K_u\to\infty\,, \tag{2.34}$$

respectively. The appropriate expression for C_1 can be substituted into the equations for the stresses and strains, in order to calculate and then minimise the strain energy.

(c) Identifying stable configurations

All stress- and strain resultants are known and, hence, the bending and stretching energy components, $\mathit{\Pi}_B$ and $\mathit{\Pi}_S$, respectively, which include the spring contributions, can be calculated via

$$\begin{aligned}\mathit{\Pi}_B &= \frac{1}{2}\int_\Omega (\hat\kappa_r m_r + \hat\kappa_\theta m_\theta)\,\mathrm{d}A \;+ \pi a K_\varphi \hat\varphi_r^2\,\big|_{\rho=1} = \pi\int_0^a (\hat\kappa_r m_r + \hat\kappa_\theta m_\theta)\,r\,\mathrm{d}r + \pi a K_\varphi\hat\varphi_r^2\,\big|_{\rho=1}\,,\\ \mathit{\Pi}_S &= \frac{t}{2}\int_\Omega (\varepsilon_r\sigma_r + \varepsilon_\theta\sigma_\theta)\,\mathrm{d}A \;+ \pi a K_u \hat u_r^2\,\big|_{\rho=1} = \pi t\int_0^a (\varepsilon_r\sigma_r + \varepsilon_\theta\sigma_\theta)\,r\,\mathrm{d}r + \pi a\,K_u u_r^2\,\big|_{\rho=1}\,.\end{aligned} \tag{2.35}$$

The integrals are solvable since all expressions are derived from polynomials. Load-free equilibrium configurations are found via stationary points of the total energy potential, $\mathit{\Pi} = \mathit{\Pi}_B + \mathit{\Pi}_S$, where

$$\nabla_\eta \mathit{\Pi} = 0\,. \tag{2.36}$$

∇_η is the differential operator with respect to the n degrees-of-freedom, η_i . These configurations are stable if, and only if, all eigenvalues of the strain energy function are positive, which is assured

by a positive definite Hessian matrix of stiffness, **H**, where

$$H_{ij} = \frac{\partial^2 \Pi}{\partial \eta_i \, \partial \eta_j} \, . \tag{2.37}$$

For a moderate compaction of notation, the following dimensionless parameters are used:

$$\rho = \frac{r}{a} \qquad \omega = \frac{w}{t} \qquad k = \kappa \cdot \frac{a^2}{t} \qquad K_U = \frac{K_u \, a}{E \, t} \qquad K_\phi = \frac{K_\varphi \, a}{E t^3} . \tag{2.38}$$

3. Results

Recall that the first example is a spherical cap supported on rollers according to the boundary conditions in Eqn (2.16*a*). The second is another spherical cap connected to ground by in-plane springs, Eqn (2.16*b*), and the third is a non-uniformly curved cap with initial deflection given by Eqn (2.14*b*) and supported by both extensional and rotational spring supports, Eqn (2.16*c*). For all cases, the variation with key physical parameters is established as a function of the number of degrees-of-freedom whilst comparing their accuracy to finite element results.

Finite element simulations were conducted with the commercial package ABAQUS [29] using a quasi-static implicit dynamic analysis. Only one quarter of the shell was modelled, with biaxial symmetry applied to over 600 elements and the following parameters: $E = 10^7$, $t = 0.01$, $a = 1$, and density equal to 10^{-5}; *c.f.* Sobota & Seffen [33] for details. Mesh refinement of randomly picked samples did not lead to any changes in the critical properties.

(a) Roller supported spherical cap

The critical dimensionless height, $\omega^0_{M\,Crit}$, required to trigger bistable inversion is shown in Fig. 4 as a function of the Poisson's ratio. The range of ν is governed by naturally stable limits of $\nu = -1$ and $\nu = 0.5$ for isotropic materials: for homogeneous shells, the Young's modulus does not affect the critical geometry. Figure 4(a) first compares results from previous studies to finite elements for the sake of revision before divulging our predictions in Fig. 4(b). Although we do not plot them, the results for the uniform curvature assumption in Vidoli [17] and in Seffen & McMahon [26] are therefore identical to the current case using $\hat{w} = (1 - \rho^2)\, \hat{w}_M$ where $(\omega^0_{M\,Crit})^2 = 16/(1-\nu)$. More interestingly, our single degree-of-freedom solution with quadratically varying curvature (QVC) which satisfies the boundary conditions exactly can be shown to be

$$\left(\omega^0_{M\,Crit}\right)^2 = \frac{160 \left[-9\nu^5 - 211\nu^4 - 1986\nu^3 - 9486\nu^2 - 23221\nu - 23583\right]}{27\nu^7 + 691\nu^6 + 7527\nu^5 + 43967\nu^4 + 138001\nu^3 + 184089\nu^2 - 64915\nu - 309387} \, . \tag{3.1}$$

The equivalent expression for two- and three degrees-of-freedom are not compactly expressed, as noted before. All models yield the same rising trend in $\omega^0_{M\,Crit}$ with the Poisson's ratio in Figs 4(a) and (b), where an initial height-to-thickness ratio of at least six guarantees bistable inversion irrespective of ν. The QVC model of Vidoli [17] shows a better approximation of the FE solution for positive Poisson's ratios in Fig. 4(a) whilst our QVC results in Fig. 4(b) are superior for negative ratios, which may be exhibited, say, by auxetic materials. Wittrick *et al.* [2] deduce that the critical height must exceed $\omega^0_{M\,Crit} = \sqrt{23.25} = 4.82$ for $\nu = 1/3$ and $\omega^0_{M\,Crit} = \sqrt{19} = 4.36$ for $\nu = 1/4$; our QVC model returns lower values of 4.13 and 3.92, respectively. Even though Mansfield [14] provides a closed-form solution of $(\omega^0_{M\,Crit})^2 = 4(14 + 2\nu)/(1 - \nu)$ for the different problem of a lenticular shell with tapering thickness, his results are presented in Fig. 4(a) because, astonishingly, his solution predicts the critical initial deflection precisely ($\pm 0.39\,\%$) for $\nu \geq 0$, but for negative Poisson's ratios the deviations rise up to 12.8%. When we increase the number of degrees-of-freedom to three, we find a better approximation of $\omega^0_{M\,Crit}$ than found so far in literature, with a maximum deviation of 0.67% from the FE results in Fig. 4(b) for all values of ν.

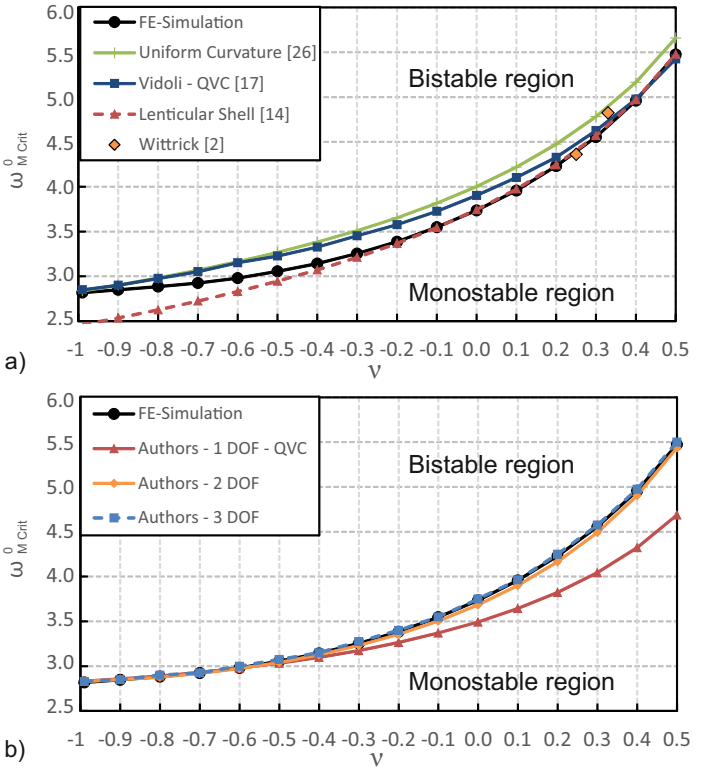

Figure 4. Dimensionless critical initial midpoint deflection $w^0_{M\,Crit}$ for inducing bistable inversion of a shallow spherical cap with respect to Poisson's ratio, ν. a) Comparison of different models in key studies; b) current models with up to three degrees-of-freedom.

(b) Spherical cap with extensional spring supports

We first set the Poisson's ratio to be 0.5 because this correlates to the *worst* case in Fig. 4 in terms of the accuracy of our QVC model for a roller supported cap. The performance of this model in the present case is indicated in Fig. 5 along with uniform curvature predictions (*c.f.* remark 2), which is also a single degree-of-freedom approach. Closed-form solutions of the critical bistable height, $\omega^0_{M\,Crit}$, have been obtained for both approaches, where the less complex UC solution reads as:

$$\left(\omega^0_{M\,Crit}\right)^2 = \frac{16}{1-\nu} \cdot \frac{1+(1-\nu)\,K_U}{1+(7-\nu)\,K_U}\,, \tag{3.2}$$

which converges to the solution of Seffen & McMahon [26] for $K_U = 0$, and to $16/(7-v)$ when $K_U \to \infty$.

The reason for including the simpler UC model is now apparent in Fig. 5 because it yields a *better* approximation of the critical geometry than the QVC model and is surprisingly close to the FE trend. However, Sobota & Seffen [25] show that this holds only for the *ratio* of bending- to stretching energies—that the close accuracy of the UC model is fortuitous, and that our single degree-of-freedom QVC model gives more accurate variations of the stress resultants. The predictions from using two- and three degrees-of-freedom are also plotted, and are almost identical to the FE solutions with maximum absolute deviations of 0.78% and 0.73%, respectively.

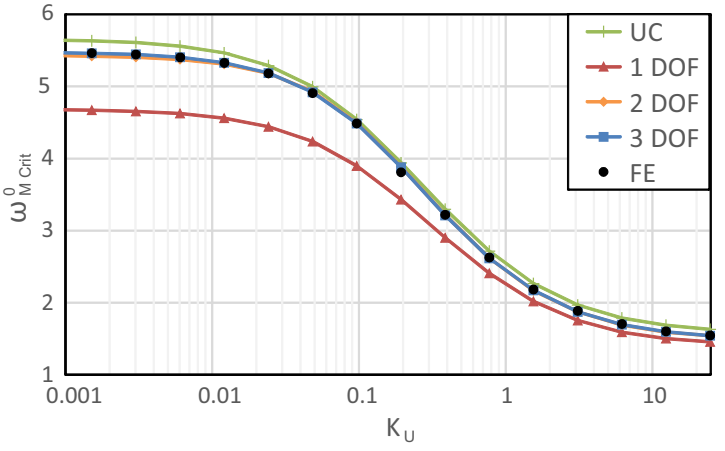

Figure 5. Dimensionless critical initial midpoint deflection $w^0_{M\,Crit}$ for bistability of a shallow spherical cap supported on extensional springs of stiffness K_U, with $\nu = 0.5$.

When K_U is small, in-plane displacements of the boundary are largely unrestricted, and the cap tends towards being roller supported, Eqn (2.16*a*). The most accurate prediction of the associated critical height is 5.5 times the thickness, which matches that in Fig. 4. As K_U increases, the critical height decreases, moreover, at $K_U \approx 1$ we observe that $\omega^0_{M\,Crit}$ falls below its previous minimum value of 2.8 in Fig. 4 for the *lowest* Poisson's ratio value: by stiffening the cap edge, the critical height can be smaller than that of the first case in view of promoting bistability. A discernible lower bound of $\omega^0_{M\,Crit} = 1.5$ arises when $K_U \gtrapprox 10$ which corresponds to an equivalent spring stiffness of at least $10Et/a$ acting on a length of $2\pi a$. When K_U becomes larger, in-plane boundary displacements are increasingly resisted, and the cap is supported in a manner akin to a fixed pinned support, Eqn (2.16*d*).

The detailed dependency on Poisson's ratio is given in Fig. 6(a), where a similar accuracy is confirmed from using three degrees-of-freedom. The variation in critical height is now plotted as a "landscape" with respect to ν and to K_U. Its discrete contours in Fig. 6(b) allow values of $\omega^0_{M\,Crit}$ to be read directly (say, for design applications); alternatively Eqn (3.2) can be used within an accuracy of 8% by comparison.

We impose the same range for K_U from Fig. 5, noting little variation in $\omega^0_{M\,Crit}$ beyond $K_U = 10$. We plot against the logarithm of spring stiffness for compactness but this also allows to infer robustly the asymptotic performances. For the case of a roller support ($K_U \to 0$), the critical heights are largest and the variation with Poisson's ratio is the most distinct. As K_U increases, $\omega^0_{M\,Crit}$ generally decreases and the Poisson effect diminishes, suggesting that bistability is now dominated by geometrical effects. Such behaviour is not surprising from what is known about the bistability of a simpler curved *beam*[6]. Whilst the beam is bistable if the ends are pinned to ground and $\omega^0_M \geq 1.15$, it is always monostable if one end is able to move horizontally; and bistability can be restored if both ends are connected by a horizontal spring of sufficient stiffness, where the critical midpoint deflection of the beam decreases with increasing spring stiffness. Within the current approach, these tendencies are *quantified* for shells: depending on the Poisson's ratio, the critical initial height for a roller supported cap must between two- and four times larger than that of a fixed pinned cap.

Out of interest, we have performed separate FE analysis of other shells with rhomboidal and elliptical planforms of aspect ratios up to 7:1. Their initial shapes conform to bi-directional sinusoidal profiles with fixed pinned supports along their boundary plane. For both types of shell, we find that the critical bistable height lies in the range $1.45 < \omega^0_{M\,Crit} < 2$ provided $\nu > 0$ for the rhombuses and independently of ν for the ellipses. These limits are similar to those found

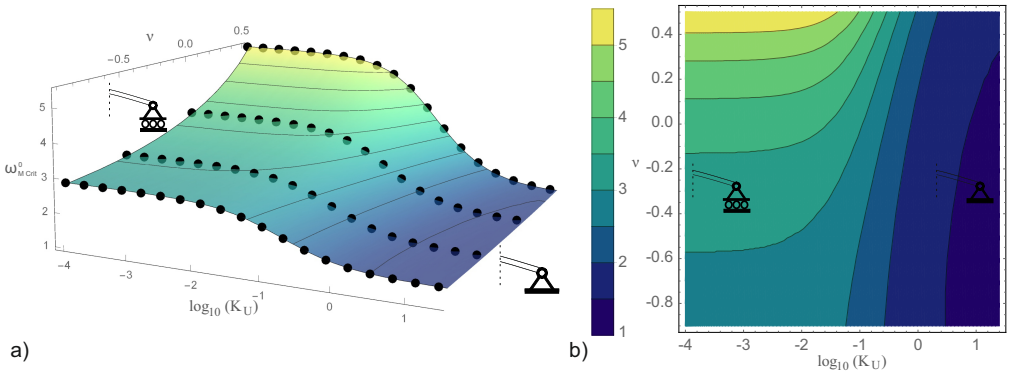

Figure 6. Dimensionless critical initial midpoint deflection $w^0_{M\,Crit}$ for bistability of a shallow spherical cap supported on extensional springs. a) Comparison of FE results with analytical model using three polynomial degrees-of-freedom: $w^0_{M\,Crit}$ *vs* spring-stiffness, $\log(K_U)$, and Poisson's ratio, ν. Dots indicate results from FE simulations, which virtually "float" on the surface such is the accuracy of correlation, and lines are contour intervals of $w^0_{M\,Crit}$ of 0.5. When K_U is large, the edge of cap tends towards being a fixed pinned support, as shown, and when K_U is very small, we have a roller support. b) Top view with discrete colouring between contours.

in Fig. 5 as K_U becomes large, which suggests a universal height for bistability of around two thicknesses for this type of boundary connection irrespective of the planform shape.

(c) Non-uniformly curved shell with extensional and rotational spring supports

The UC approach is no longer suitable since neither the initial shape nor the deformation field have uniform curvature, recall Eqn (2.14*b*). Sample results for different degrees-of-freedom are displayed in Fig. 7 and compared to FE predictions for the case of $K_U = 1$ and $\nu = 0.3$. The range of rotational stiffness, K_ϕ, is specified from a very small value up to $K_\phi \approx 100$, where each variation in $\omega^0_{M\,Crit}$ reaches an apparent upper bound. Whilst models with one or two degrees-of-freedom are suitable for the range of $K_\phi < 1$, the error in $\omega^0_{M\,Crit}$ increases considerably with increasing rotational stiffness. At least three degrees-of-freedom are therefore needed for a good approximation ($< 2\%$) of the FE solution. The corresponding variation in the critical bistable height due to both variations in the extensional and rotational spring stiffnesses is given in Fig. 8 for $\nu = 0.3$.

Note that the axes variation for K_U has been reversed in Fig. 8(a) for a more open perspective of the solution landscape, and that larger values of K_U have been used compared to previous figures, in order to reveal the pertinent variation. The landscape topography is clearly non-linear, for example, $\omega^0_{M\,Crit}$ typically decreases with K_U increasing for a given K_ϕ but the trend in general reverses for K_ϕ varying. The behaviour for K_U varying mirrors that of the second example despite it having a different initial shape and no rotational support: that by resisting in-plane edge displacements, bistability can prevail. A rotational spring tends to revert the shell by definition since it applies an edge bending moment in the sense of the initial shape. So, by reducing the applied moment by decreasing K_ϕ, we also promote bistability. Closer inspection reveals an anomalous "dip" in the downwards trend of $\omega^0_{M\,Crit}$ with respect to K_ϕ for the largest values of K_U. Importantly, the critical height is lowest for a non-zero value of K_ϕ (≈ 0.39), which suggests that a moderate value of rotational spring stiffness benefits bistability—here, this stiffness is equivalent to $4.26D/a$. We surmise that this attests to the highly non-linear interaction between stretching and bending in shells, and to their sensitivity to edge effects, which we hope to quantify in further study. A discrete contour plot is also given

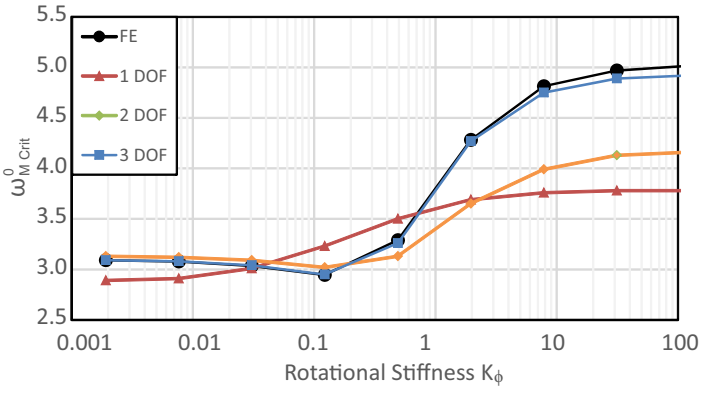

Figure 7. Dimensionless critical initial midpoint deflection $\omega^0_{M\,Crit}$ of a non-uniformly curved shell, Eqn (2.14*b*), supported on extensional (K_U) and rotational (K_ϕ) springs. Convergence to FE results occurs when the number of degrees-of-freedom are increased, for $K_U = 1$ and $\nu = 0.3$.

in Fig. 8(b) where the asymptotic support conditions are also indicated in the four corners of the plot. In the sense of in-plane *vs* rotational freedoms, these are fixed-fixed (K_U & $K_\phi \to \infty$), fixed-free ($K_U \to \infty$, $K_\phi \to 0$), free-fixed ($K_U \to 0$ $K_\phi \to \infty$) and free-free (K_U & $K_\phi \to 0$).

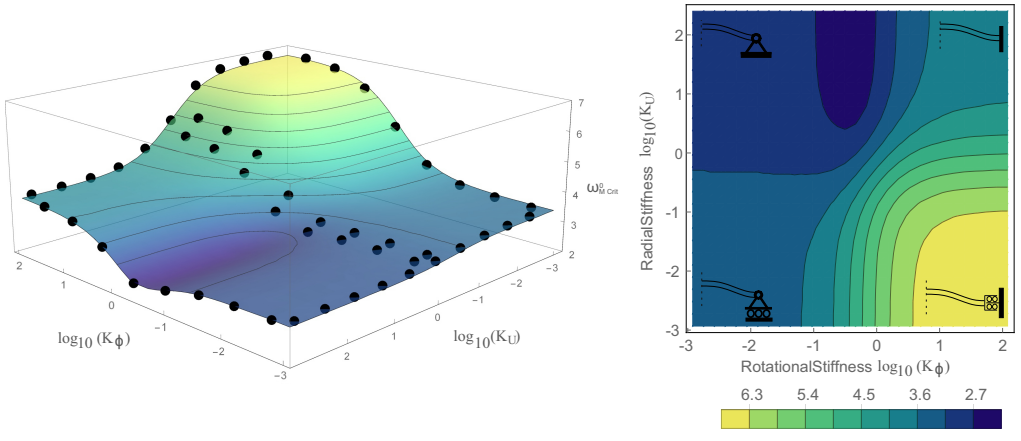

Figure 8. Dimensionless critical initial midpoint deflection $\omega^0_{M\,Crit}$ for a non-uniformly curved shell supported on extensional (K_U) and rotational (K_ϕ) springs. a) Comparison of FE results (dots) with analytical model using three degrees-of-freedom, with $\nu = 0.3$. b) Top view of the same plot with discrete colouring and indicating the asymptotic support conditions for extreme values of spring stiffnesses.

(d) Final remarks

Because our deflection field comprises a clamped deformation mode and a hinged (pinned) mode, we cannot capture an ideal clamped support outright because the hinged mode is inherently coupled to the overall solution. We can only *approach* an ideal clamp by setting K_ϕ to be a very large finite value. In the earlier derivation, the total strain energy, Π, ultimately expresses K_ϕ to the fourth power (but not so for K_U), which compounds further the effect that large

values of K_ϕ can have upon the numerical solution procedure, especially when solving for the eigenvalues of the Hessian matrix, Eqn (2.37). A sensible limit for K_ϕ should be correlated to the range of numerical floating-point precision of the particular software package. For basic packages, this range is 16 decimal places (or "16-point"), so setting $0 < K_\phi^4 < 10^{16}$ should not produce inaccuracies: we have used the general analysis software package Mathematica [34], which can express much higher precision levels, and we find our results here (up to $K_\phi \leq 10^4$) to be indistinguishable from those of Sobota & Seffen [25] who deal with a clamped support shell from the outset.

We have chosen specific initial shapes because of their ubiquity in other studies. Other shape profiles are indeed amenable to our method, but we have to consider the nature of our approach, which differs from FE analysis: both methods can theoretically lead to "false negatives" or to "false positives", but the first is more likely in FE analysis, whilst our choice *not* to linearise the work equation increases the possibility of the latter. Using FE, we cannot exclude the possibility of alternative equilibrium states since the linear stiffness matrix would require us to evaluate an infinite number of possible combinations. However, because of linearisation, the problem becomes amenable to a numerical solution process even for discretisations with a large number of degrees-of-freedom. The current method considers a non-linear stiffness matrix, $\mathbf{H}$, which implies that computational efficiency limits us to a few degrees-of-freedom; hence, our set of shape functions is not necessarily accurate enough. This problem can be illustrated by the example of a uniformly curved cap now clamped on its edge, where the gradient remains non-zero for all time. Although we never observed bistable behaviour in finite element simulations for a wide range of initial geometries, our theoretical analysis suggests its feasibility. In the FE simulations, we observe that the radial curvature becomes highly concentrated just before the clamped edge, which gives way to a large restoring moment despite the "holding" effects of significant in-plane circumferential tension. Our lower-order models fail to capture the strongly curved domain next to the edge, but simply increasing the order is not a viable solution approach because the midpoint deflections and, more importantly, deflection gradients (recall $\mathrm{d}w/\mathrm{d}r \ll 1$), increase beyond the limits acceptable for shallow shell behaviour and thus beyond the scope of this study.

4. Summary

We have addressed the bistable properties of an initially stress-free shell supported on its circular edge by extensional and rotational springs. Our analytical solutions have been derived from a Rayleigh-Ritz method with a polynomial series up to four degrees-of-freedom. The Föppl-von Kármán compatibility equation has been satisfied by making use of Gauss's Theorema Egregium, and the connection between the Gaussian curvature and the Airy stress function has been established independently of the in-plane boundary conditions. Solutions for the uniform- and quadratically varying curvature approaches have been captured in closed form and are accurate for most design processes when the edge is hinged. In all results, having a radial spring stiffness promotes bistability; in the example of a roller supported cap, the critical initial midpoint deflection for bistability has been shown to be between two and four times higher than that of the same pinned cap but where radial edge displacements are now prevented. Whilst the response of the former was highly dependent on the Poisson's ratio, the latter was almost independent of ν. Incorporating a rotational spring stiffness has shown that the response of the structure produces a strongly non-uniform Gaussian curvature field, and therefore, higher-order models with at least three degrees-of-freedom are needed to capture the bistable response. It has been demonstrated that a horizontally immoveable boundary in combination with a specific value of rotational spring stiffness, which is not an extreme case, can minimise the critical initial height needed to achieve bistability. Compared to structures with hinged edges, fully clamped boundaries tend to prevent bistability.

Data accessibility statement

This work does not have any physical experimental data. The essential codes for finite element analysis[33] via ABAQUS[29] and for solving the analytical models[35] via Mathematica[34] are available in the cited repositories and for open consultation, which also contain the data for generating the results presented in Figs 4-8.

Competing interests statement

The authors declare they have no competing interests.

Authors' contributions

PMS and KAS conceived the methodology, interpreted the results, and wrote the paper in equal measure. PMS performed the finite element simulations and wrote the Mathematica code, all in consultation with KAS. Both authors gave final approval for publication.

Funding

PMS is grateful to the Friedrich-Ebert-Foundation for their financial support; this work was otherwise not supported by funding from any other agency.

Acknowledgements

Both authors are grateful to Prof. Stefano Vidoli for explaining his QVC model at the start of study.

Appendix

For a n degree-of-freedom model, the current radial and circumferential curvatures, κ_r and κ_θ, respectively, read:

$$\begin{aligned}
\kappa_r &= \kappa_r^0 + \hat{\kappa}_r^h + \hat{\kappa}_r^c \\
&= \kappa_r^0 + \sum_{i=1}^{n} \left[\frac{1}{1+\nu} - \frac{1+2i}{1+2i+\nu}\rho^{2i} \right] \frac{\eta_i}{a^2} - 4\left(3\rho^2 - 1\right) \frac{K_\varphi\, a}{8D} \sum_{i=1}^{n} \left[\frac{1}{1+\nu} - \frac{2i}{1+2i+\nu} \right] \frac{\eta_i}{a^2}\,, \\
\kappa_\theta &= \kappa_\theta^0 + \hat{\kappa}_\theta^h + \hat{\kappa}_\theta^c \\
&= \kappa_\theta^0 + \sum_{i=1}^{n} \left[\frac{1}{1+\nu} - \frac{1}{1+2i+\nu}\rho^{2i} \right] \frac{\eta_i}{a^2} - 4\left(\rho^2 - 1\right) \frac{K_\varphi\, a}{8D} \sum_{i=1}^{n} \left[\frac{1}{1+\nu} - \frac{2i}{1+2i+\nu} \right] \frac{\eta_i}{a^2},
\end{aligned} \tag{A.1}$$

where the initial values κ_r^0 and κ_θ^0 follow from Eqn (2.14). The change in Gaussian curvature according to Eqn (2.11) is found to be:

$$\begin{aligned}
\hat{g} = &\left[\kappa_r^0 + \sum_{i=1}^{n} \left[\frac{1}{1+\nu} - \frac{1+2i}{1+2i+\nu}\rho^{2i} \right] \frac{\eta_i}{a^2} - 4\left(3\rho^2 - 1\right) \frac{\hat{w}_M^c}{a^2} \right] \times \\
&\left[\kappa_\theta^0 + \sum_{i=1}^{n} \left[\frac{1}{1+\nu} - \frac{1}{1+2i+\nu}\rho^{2i} \right] \frac{\eta_i}{a^2} - 4\left(\rho^2 - 1\right) \frac{\hat{w}_M^c}{a^2} \right] - \kappa_r^0 \kappa_\theta^0\,,
\end{aligned} \tag{A.2}$$

where $\hat{w}_M^c$ is defined in Eqn (2.26). The corresponding α_i-terms for Eqn (2.12), where $2p - 4 = 4n$, for three degrees-of-freedom and a uniformly curved initial shape [*c.f.* Eqn (2.14*a*)] read:

$$
\begin{aligned}
\alpha_0 &= \frac{\left(2\left(\eta_1+\eta_2+\eta_3+4(\nu+1)\hat{w}_M^c\right)+(\nu+1)w_M^0\right)^2}{4\,a^4\,(\nu+1)^2}\,,\\
\alpha_2 &= -\frac{2\left[\eta_1+4(\nu+3)\hat{w}_M^c\right]\left[2\left(\eta_1+\eta_2+\eta_3+4(\nu+1)\hat{w}_M^c\right)+(\nu+1)w_M^0\right]}{a^4\,(\nu+1)(\nu+3)}\,,\\
\alpha_4 &= \frac{3}{a^4}\left(\frac{8\eta_1\hat{w}_M^c}{\nu+3}-\frac{8\eta_2\hat{w}_M^c}{\nu+5}+16w_M^{2C}+\frac{\eta_1^2}{(\nu+3)^2}-\frac{2\eta_2\left(\eta_1+\eta_2+\eta_3\right)}{(\nu+1)(\nu+5)}-\frac{\eta_2 w_M^0}{\nu+5}\right)\,,\\
\alpha_6 &= \frac{4}{a^4}\left(\frac{8\eta_2\hat{w}_M^c}{\nu+5}-\frac{8\eta_3\hat{w}_M^c}{\nu+7}+\frac{2\eta_1\eta_2}{\nu^2+8\nu+15}-\frac{2\eta_3\left(\eta_1+\eta_2+\eta_3\right)}{(\nu+1)(\nu+7)}-\frac{\eta_3 w_M^0}{\nu+7}\right)\,,\\
\alpha_8 &= \frac{5}{2\,a^4}\left(\frac{4\eta_3\left(4(\nu+3)\hat{w}_M^c+\eta_1\right)}{(\nu+3)(\nu+7)}+\frac{2\eta_2^2}{(\nu+5)^2}\right)\,,\\
\alpha_{10} &= \frac{1}{a^4}\frac{12\eta_2\eta_3}{(\nu+5)(\nu+7)}\,,\quad \alpha_{12}=\frac{1}{a^4}\frac{7\eta_3^2}{(\nu+7)^2}\,,\quad \alpha_1=\alpha_3=\alpha_5=\alpha_7=\alpha_9=\alpha_{11}=0\,.
\end{aligned}
\tag{A.3}
$$

For non-uniformly curved initial shapes defined in Eqn (2.14*b*), the corresponding α-terms of a model with three degrees-of-freedom are calculated to be:

$$
\begin{aligned}
\alpha_0 &= \frac{\left(4(\nu+1)\hat{w}_M^c+\eta_1+\eta_2+\eta_3+4(\nu+1)w_M^0\right)^2}{a^4\,(\nu+1)^2}\,,\\
\alpha_2 &= -\frac{4\left(4(\nu+3)\hat{w}_M^c+\eta_1+4(\nu+3)w_M^0\right)\left(4(\nu+1)\hat{w}_M^c+\eta_1+\eta_2+\eta_3+4(\nu+1)w_M^0\right)}{a^4\,(\nu+1)(\nu+3)}\,,\\
\alpha_4 &= \frac{3}{2\,a^4}\left(\frac{16\eta_1\left(\hat{w}_M^c+w_M^0\right)}{\nu+3}+\eta_2\left[\frac{\left(\eta_1+\eta_2+\eta_3-16(w_M^0+\hat{w}_M^c)\right)}{\nu+5}-\frac{(\eta_1+\eta_2+\eta_3)}{\nu+1}\right]\right.\\
&\qquad \left.+32\left(\hat{w}_M^c+w_M^0\right)^2+\frac{2\eta_1^2}{(\nu+3)^2}\right)\,,\\
\alpha_6 &= \frac{8}{a^4}\left(\frac{4\eta_2\hat{w}_M^c}{\nu+5}-\frac{4\eta_3\hat{w}_M^c}{\nu+7}+\frac{\eta_1\eta_2}{\nu^2+8\nu+15}-\frac{\eta_3\left(\eta_1+\eta_2+\eta_3\right)}{(\nu+1)(\nu+7)}+\frac{4\eta_2 w_M^0}{\nu+5}-\frac{4\eta_3 w_M^0}{\nu+7}\right)\,,\\
\alpha_8 &= \frac{5}{2\,a^4}\left(\frac{4\eta_3\left(4(\nu+3)\hat{w}_M^c+\eta_1+4(\nu+3)w_M^0\right)}{(\nu+3)(\nu+7)}+\frac{2\eta_2^2}{(\nu+5)^2}\right)\,,\\
\alpha_{10} &= \frac{1}{a^4}\frac{12\eta_2\eta_3}{(\nu+5)(\nu+7)}\,,\quad \alpha_{12}=\frac{1}{a^4}\frac{7\eta_3^2}{(\nu+7)^2}\,,\quad \alpha_1=\alpha_3=\alpha_5=\alpha_7=\alpha_9=\alpha_{11}=0\,.
\end{aligned}
\tag{A.4}
$$

References

1 Forterre, Y., Skotheim, J. M., Dumais, J. & Mahadevan, L. How the Venus Flytrap snaps. *Nature* **433**, 421–425 (2005).

2 Wittrick, W., Myers, D. & Blunden, W. Stability of a bimetallic disk. *The Quarterly Journal of Mechanics and Applied Mathematics* **6**, 15–31 (1953).

3 Freund, L. Some elementary connections between curvature and mismatch strain in compositionally graded thin films. *Journal of the Mechanics and Physics of Solids* **44**, 723–736 (1996).

4 Betts, D. N., Kim, H. A., Bowen, C. R. & Inman, D. Optimal configurations of bistable piezo-composites for energy harvesting. *Applied Physics Letters* **100**, 114104 (2012).

5 Brinkmeyer, A., Pellegrino, S. & Weaver, P. M. Effects of long-term stowage on the deployment of bistable tape springs. *Journal of Applied Mechanics* **83**, 011008 (2016).

6 Timoshenko, S. *Theory of Elastic Stability, (2nd edition)* (McGraw-Hill Education, 1963).

7 Hyer, M. W. Calculations of the room-temperature shapes of unsymmetric laminates. *Journal of Composite Materials* **15**, 296–310 (1981).

8 Audoly, B. & Pocheau, Y. *Elasticity and Geometry: from Hair Curls to the Non-linear Response of Shells* (Oxford University Press, 2010).

9 Calladine, C. R. *Theory of Shell Structures* (Cambridge University Press, 1983).

10 Guest, S. & Pellegrino, S. Analytical models for bistable cylindrical shells. *Proceedings of the Royal Society of London A: Mathematical, Physical and Engineering Sciences* **462**, 839–854 (2006).

11 Seffen, K. A. Morphing bistable orthotropic elliptical shallow shells. *Proceedings of the Royal Society of London A: Mathematical, Physical and Engineering Sciences* **463**, 67–83 (2007).

12 Vidoli, S. & Maurini, C. Tristability of thin orthotropic shells with uniform initial curvature. *Proceedings of the Royal Society of London A: Mathematical, Physical and Engineering Sciences* **464**, 2949–2966 (2008).

13 Hamouche, W., Maurini, C., Vincenti, A. & Vidoli, S. Basic criteria to design and produce multistable shells. *Meccanica* (2016).

14 Mansfield, E. H. Bending, buckling and curling of a heated elliptical plate. *Proceedings of the Royal Society of London A: Mathematical, Physical and Engineering Sciences* **288**, 396–417 (1965).

15 Alwar, R. & Nath, Y. Application of Chebyshev polynomials to the nonlinear analysis of circular plates. *International Journal of Mechanical Sciences* **18**, 589–595 (1976).

16 Lamacchia, E., Pirrera, A., Chenchiah, I. & Weaver, P. Morphing shell structures: a generalised modelling approach. *Composite Structures* **131**, 1017–1027 (2015).

17 Vidoli, S. Discrete approximations of the Föppl–Von Kármán shell model: from coarse to more refined models. *International Journal of Solids and Structures* **50**, 1241–1252 (2013).

18 Seffen, K. A. & Vidoli, S. Eversion of bistable shells under magnetic actuation: a model of nonlinear shapes. *Smart Materials and Structures* **25**, 065010 (2016).

19 Brunetti, M., Vincenti, A. & Vidoli, S. A class of morphing shell structures satisfying clamped boundary conditions. *International Journal of Solids and Structures* (2015).

20 Datsiou, K. C. & Overend, M. The mechanical response of cold bent monolithic glass plates during the bending process. *Engineering Structures* **117**, 575–590 (2016).

21 Alwar, R. & Reddy, B. S. Large deflection static and dynamic analysis of isotropic and orthotropic annular plates. *International Journal of Non-Linear Mechanics* **14**, 347–359 (1979).

22 Anh, V. T. T. & Duc, N. D. The nonlinear stability of axisymmetric functionally graded material annular spherical shells under thermo-mechanical load. *Mechanics of Advanced Materials and Structures* **23**, 1421–1429 (2016).

23 Dumir, P. Nonlinear axisymmetric response of orthotropic thin spherical caps on elastic foundations. *International Journal of Mechanical Sciences* **27**, 751–760 (1985).

24 Duc, N. D., Quang, V. D. & Anh, V. T. T. The nonlinear dynamic and vibration of the S-FGM shallow spherical shells resting on an elastic foundations including temperature effects. *International Journal of Mechanical Sciences* **123**, 54–63 (2017).

25 Sobota, P. M. & Seffen, K. A. Multistable slit caps. *Proceedings of the International Association for Shell and Spatial Structures (IASS)* (2016).

26 Seffen, K. A. & McMahon, R. A. Heating of a uniform wafer disk. *International Journal of Mechanical Sciences* **49**, 230–238 (2007).

27 Föppl, A. *Vorlesungen über Technische Mechanik*, vol. 5 (BG Teubner, 1907).

28 von Kármán, T. Festigkeitsprobleme im Maschinenbau, Encyclopädie der mathematischen Wissenschaften IV (1910).

29 Hibbitt, Karlsson & Sorensen. *ABAQUS/Standard User's Manual, Version 6.14*, vol. 1 (Hibbitt, Karlsson & Sorensen, 2014).

30 Timoshenko, S. & Woinowsky-Krieger, S. *Theory of Plates and Shells*, vol. 2 (McGraw-hill New York, 1959).

31 Duc, N. D., Anh, V. T. T. & Cong, P. H. Nonlinear axisymmetric response of FGM shallow spherical shells on elastic foundations under uniform external pressure and temperature. *European Journal of Mechanics-A/Solids* **45**, 80–89 (2014).

32 Zhang, Y. Large deflection of clamped circular plate and accuracy of its approximate analytical solutions. *Science China Physics, Mechanics & Astronomy* **59**, 1–11 (2016).

33 Sobota, P. & Seffen, K. Figshare repository (2017). URL https://figshare.com/s/10f43228745c412a810f.

34 Wolfram Research, Inc. *Mathematica* (Wolfram Research, Inc., Champaign, Illinois, 2016), 10.4 edn.

35 Sobota, P. & Seffen, K. Figshare repository (2017). URL https://figshare.com/s/5450680f6b09359ed211.